Journal of
Intelligent Material
Systems and Structures

Original Article

Journal of Intelligent Material Systems and Structures
2018, Vol. 29(12) 2557–2569

DOI: 10.1177/1045389X18770859
journals.sagepub.com/home/jim
SAGE

Concrete–fiber-reinforced polymer interfacial bond monitoring with self-triggering sensors

Kunal Joshi, Marquese Pollard, Andrea Chiari and Tarik Dickens

Abstract

External bonding with fiber-reinforced polymers is currently one of the most popular technologies for rehabilitation of concrete structures. However, the effectiveness of the technology largely depends on the strength of the bond between the fiber-reinforced polymer laminate and the concrete substrate. This article provides a system to monitor the loss of bond between the fiber-reinforced polymer laminate and the concrete. Fiber optic sensors are broadly accepted as a structural health monitoring device for fiber-reinforced polymer materials by integrating the sensors into the host material. A recent development in fiber optic sensor technology is the mechanoluminescence-based optoelectronic sensors. Concrete beams strengthened with multifunctional fiber-reinforced polymer laminates were tested in shear using these sensors to evaluate the bond strength of the composite system. The sensors showed response to shear stress transfer in the adhesive layer which was observed to be as low as 2 MPa. The inclusion of sensors does not affect the bond strength (3.35 MPa), for both beams with sensors and without sensors. Real-time failure detection of fiber-reinforced polymer–strengthened beams was successfully achieved in this study. In future, the scheme aims at providing a tool to reduce the response time and decision making involved in the maintenance of deficient structures.

Keywords

Adhesive layer, bond monitoring, optical fiber sensor, triboluminescence

Introduction

Adhesive bonding has been increasingly used as a mechanical fastening technique in the last decade. For many applications in the automotive, aerospace, and civil industries, it has become a popular structural strengthening, joining, or repair technique (Banea and Da Silva, 2009; Higgins, 2000; Wu and Jiang, 2013). Adhesive bonds can be used to join dissimilar materials to produce structures with higher strength and better fatigue properties than traditional fastening methods, such as mechanical bolting, riveting, and welding due to the resulting fewer stress concentrations at the interface and better load transfer characteristics. Moreover, they save manufacturing costs and result in weight savings. It has been a popular technique for the rehabilitation also called as strengthening/repairing/retrofitting of concrete structures (Teng et al., 2003). Although the technique has the above-mentioned advantages, the effectiveness of the technology largely depends on the bond strength. Furthermore, the quality of the bond also depends on the skill and expertise of the manufacturer. This has resulted in reluctance of industries to use adhesive bonding. The reluctance of industries in using adhesive bonding technique is also because so far there is no reliable in situ testing or monitoring technique that allows one to monitor the bond quality under static or dynamic loads (Abdel Wahab, 2012; Curley et al., 2000; Ehrhart et al., 2010). Many experimental techniques have been applied to characterize the mechanical behavior and evaluate damage in adhesive joint components (including Moiré interferometry (Tsai and Morton, 1995), strain gages (Shenoy et al., 2009), or digital image correlation (Comer et al., 2013)). However, these techniques provide surficial data and cannot be easily extended to study the non-uniform internal damage sites within the bonded region. Other internal bond region monitoring technique most experimented with are the fiber Bragg grating (FBG) sensors

FAMU-FSU College of Engineering and High Performance Materials Institute, Florida A&M University, Tallahassee, FL, USA

Corresponding author:
Tarik Dickens, College of Engineering and High Performance Materials Institute, Florida A&M University, 1601 S Martin Luther King Jr Blvd, Tallahassee, FL 32307, USA.
Email: dickens@eng.famu.fsu.edu

(Majumder et al., 2008); however, the technique is still undeveloped and suffers from cross-sensitivity which results in false alarms.

In this article, we address this problem and propose a technique for detecting debonding in a glue joint with focus toward debonding failure modes that occur in a strengthened concrete structure.

To begin with, we use the knowledge that debonding of the adhesive interface or cracks in the adhesive layer leads to a redistribution of the shear stress profile in the bond layer. Therefore, a method that allows one to monitor the behavior of the adhesive interface will provide information about the damage state condition. More specifically, we report the real-time damage sensing capability that is provided by the integrated triboluminescent (TL) fiber optic sensors (Okoli and Olawale, 2016) that are placed in the concrete-composite interface. The sensors do not require any additional source of energy to generate information from the host structure. This makes it a self-triggering sensor when compared to traditional strain gages or more recently used FBG sensors, wherein an external source of energy in the form of electrical energy and photonic energy is required (Majumder et al., 2008). We have performed single lap shear tests (shown in section "Experimentation"), which is ASTM-recommended tests (ASTM D5868-01, 2014) to evaluate the bond stresses and bond characteristic in a bonded joint. The sensor is capable of monitoring the initiation and growth of debonding in the adhesive layer. Finally, we conclude on the potential of our sensing system for long-term in situ debond monitoring of adhesively bonded composite in civil infrastructure.

Theory

Triboluminescence

Triboluminescence (TL) is an optical phenomenon that occurs in solids and is characterized by emission of photons when the chemical bonds in the solid are broken when it is scratched, crushed, or pulled apart (Figure 1).

Mechanoluminescence is a term used when the emissions are a result of mechanically induced stress or energy (Sharma et al., 2011). Chandra (2011) classified these mechanoluminscent emissions into three categories, namely, (1) elastico, (2) plastico, and (3) fracto-luminescence. Elastico-TL is luminescence produced during the elastic deformation of solids, where neither fracture nor plastic deformation is required. This can be by mechanical or electrostatic interaction of dislocations with defect centers or by thermal excitation in the stressed regions of solids (Chandra, 1998). Plastico-TL is luminescence produced during plastic deformation of solids where a fracture is not required. It can be excited by the mechanical or electrostatic interaction of dislocations with defect centers, electrification of crystal surfaces by the movement of charged dislocations, or thermal excitation in the stressed regions of solids such as colored alkali halides, II-VI compounds, alkaline-earth oxides, and metals (Chandra, 1998). Fracto-TL is luminescence produced due to the creation of new surfaces during the fracture of solids. ZnS:Mn has displayed the maximum triboluminescence yield out of any other existing crystals (Xu et al., 1999). In ZnS:Mn crystals, it has been reported that the TL is due to the unpinning of dislocations from manganese ions (Alzetta et al., 1970). At the start of the loading σ, the dislocation loops between defects begin to bow out, up to the point where an unpinning of dislocations from defects takes place. This breakdown occurs when σ acting on the dislocation is equal to the Cotrell bonding forces (Alzetta et al., 1970). Application of this phenomenon in adhesive layer monitoring is a technique that has not been investigated before. In this work, we use the knowledge of triboluminescence in detecting adhesive layer failure using a poly(methyl methacrylate) (PMMA)-based optical fiber. The optical fiber is functionalized with a solution of ZnS:Mn crystals (2–25 μm in size) purchased from Phosphor technology, UK and DYMAX© UV curable resin as shown in Figures 2 and 3.

The TL coating acts similar to a sensory receptor in the human nervous system, where as the optical fiber is the transport medium for the TL optical signals to photodetectors. The advantages of optical fiber sensors include small size, low weight, immunity to electromagnetic fields, high voltage, corrosion resistance, and compatibility with different materials. In traditional optical fiber sensing technologies such as FBG sensors

Figure 1. Examples of light emissions from highly efficient triboluminescent materials (Sage et al., 2001).

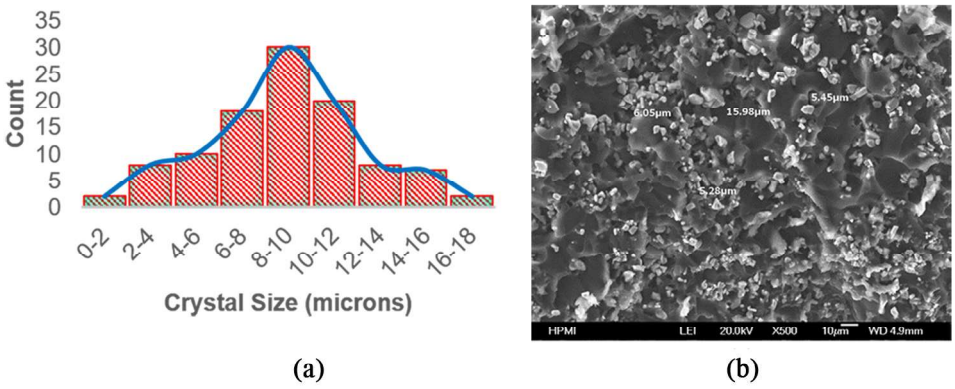

Figure 2. (a) SEM of 150 × 150 μm ROI. (b) Crystal size distribution.

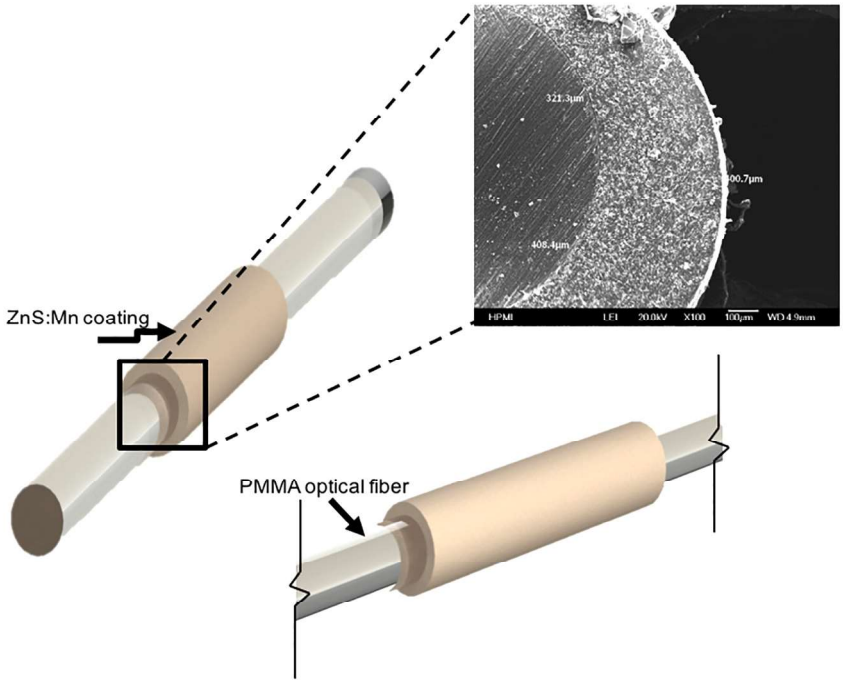

Figure 3. A typical TL sensor.

and Brillouin Optical Time Domain Reflectometer (BOTDR) sensors, a light pulse is sent through the optical fiber from one end after which one can receive information from the sensor. However, in the TL sensor, there is no external light source required as the light emissions are generated from the crystal coating itself. Thus, the mechanism of light transfer is through side coupling as compared to end coupling in traditional sensors (Figure 4). It has been explained by Chandra (1998) that the elasto-luminescence of a single ZnS:Mn crystal occurs at a pressure of 1 MPa. Thus, it can be assumed that the sensitivity of the TL sensor is as low as 1 MPa which is lower than most of the commercially available stress sensors. The sensors have shown great potential of damage detection when embedded in fiber-reinforced polymer (FRP) composites (Joshi et al., 2015a, 2015b); however, the goal of this study is to investigate the performance of the TL sensors in the adhesive layer of an externally strengthened concrete member.

Stress transfer mechanism

In an adhesively bonded FRP–concrete system, the adhesive layer is a critical component as all the loads from the concrete beam are transferred to the composite through this layer. Because of which, there are several failure modes associated with this system. The failure modes are mainly classified as (1) cover delamination, (2) FRP debonding, and (3) FRP rupture as shown in Figure 5(a). The debonding failure modes are

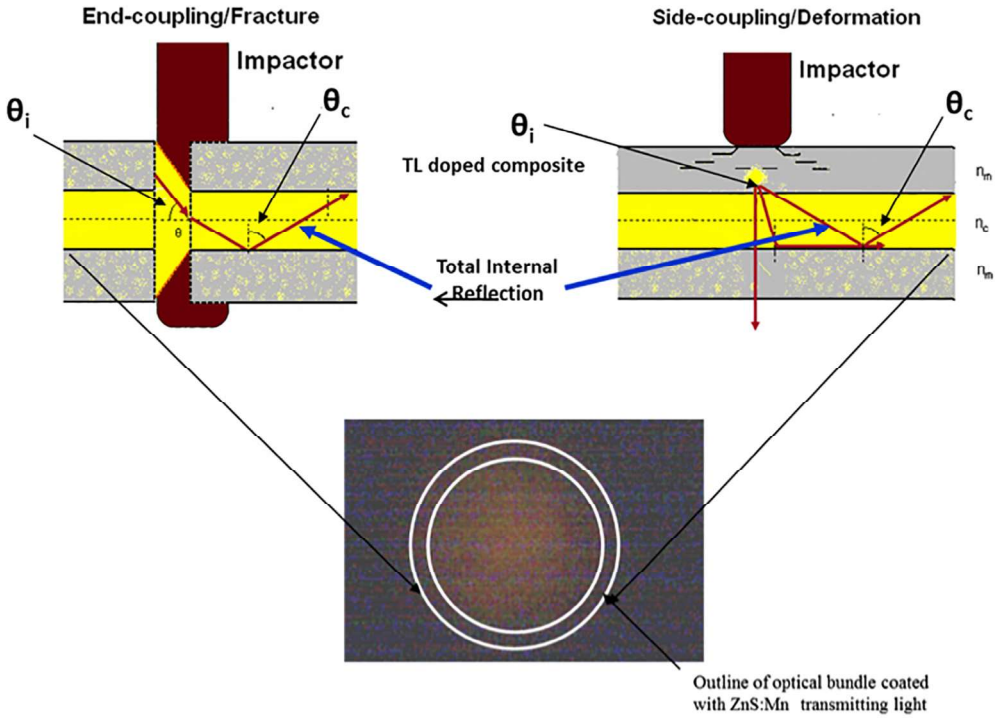

Figure 4. Total internal reflection of light guided along an optical fiber path (Dickens et al., 2008).

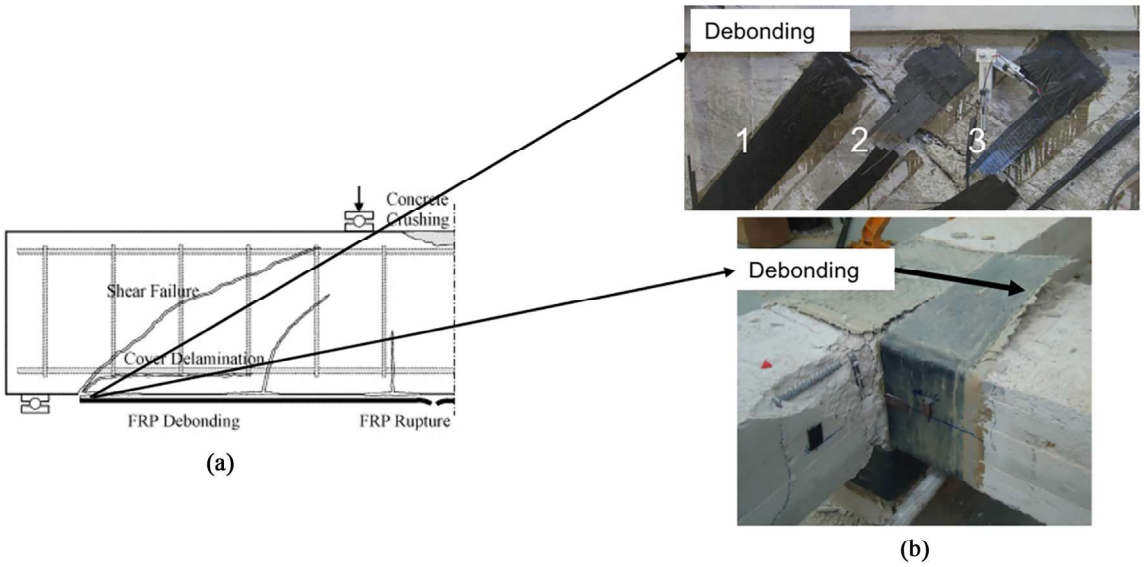

Figure 5. (a) Failure modes in a FRP-concrete system and (b) illustration of debonding failure modes (Wu et al., 2002).

further classified as adhesion failure mode where the failure occurs at the FRP-adhesive interface or the concrete-adhesive interface, and cohesion failure mode where the failure occurs in the adhesive layer itself. Both these failure modes are unwanted failure modes as this results in the concrete not being able to utilize the maximum strength that the FRP can offer. Lau et al. (2001) developed a theoretical model (Figure 6) for flexurally strengthened concrete beams where they explained that the forces experienced by the adhesive layer are a result of energy absorption that results in high shear stresses and shear deformations. The shear stresses (τ_a) in the adhesive layer are given by equation (1) (Lau et al., 2001)

$$\tau_a(x) = \frac{G_a}{t_a}[u_p(x) - u_c(x)] \quad (1)$$

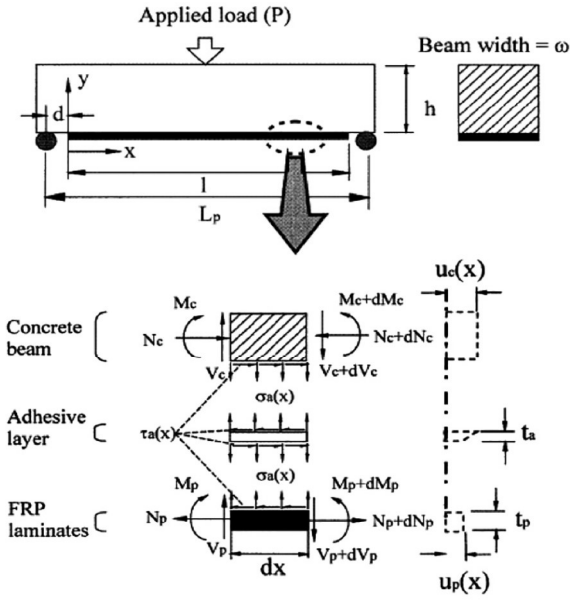

Figure 6. Stress transfer mechanism in the adhesive layer as explained by Lau et al. (2001).

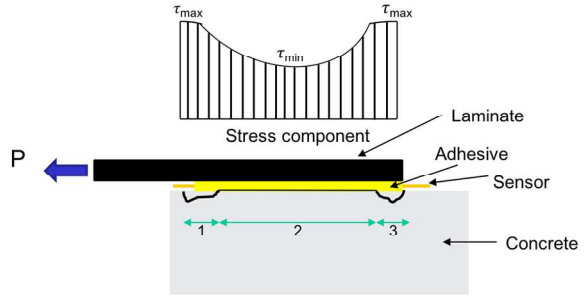

Figure 7. A typical single lap shear test, also showing the stress component.

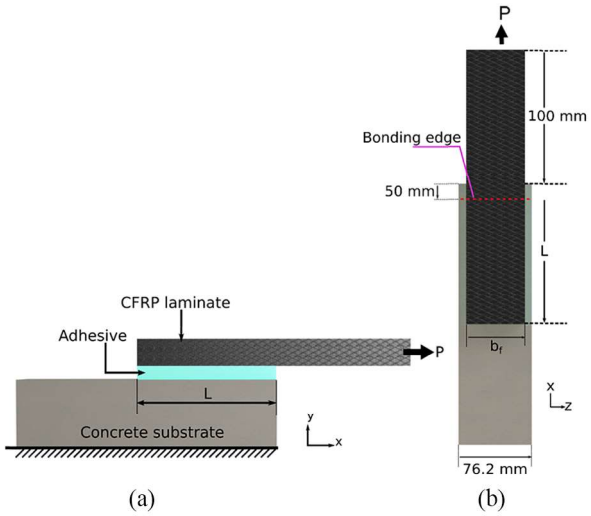

Figure 8. Sample specifications and test plan: (a) side view and (b) top view.

where G_a is the adhesive shear modulus, t_a is the adhesive thickness, $u_p(x)$ is the displacement of the FRP laminate, and $u_c(x)$ is the displacement of the concrete beam. The single lap shear tests provide direct shearing of the adhesive layer and give a better estimate of its performance. The stress concentrations in a single lap shear tests keep redistributing itself as the crack propagates toward the end of one bonded region to the other in three phases (Figure 7). Using this knowledge, we have placed the TL sensor in the adhesive layer (explained in section "Experimentation") to investigate the shear stress-induced sensor response.

Experimentation

In a single lap shear test, the stress concentrations are the highest at the ends of the bonded region and lowest at the center as shown in Figure 7. These tests are characterized by three phases of failure modes where the first failure mode occurs at the boundary condition of the concrete and represents about 10%–15% of the test cycle. The failure phases two and three represent about 70%–85% of the test cycle where the crack propagates from the first phase into the adhesive layer or one the interfaces eventually leading to complete debonding at the end of bonded region(Smith and Teng, 2002a, 2002b; Yuan et al., 2004). Considering the stress component, the location of the TL sensor was chosen to be at the center of the adhesive layer aligned along the length of the concrete beam so that the sensor is able to cover the entire stress region.

The samples were designed such that they are able to be used in the 858 mechanical testing system from MTS Corporation. The sample design is shown in Figure 8. The concrete beams were manufactured from a high-strength concrete pre-mix from Sacrete. The beams had a 28-day compressive strength of 27.8 MPa. The cross-sectional dimensions of the manufactured concrete beam were 3 in × 3 in (76.2 mm × 76.2 mm) with a length of 12 in (304.8 mm). IM6 plain weave carbon fiber fabric was used in this work with a nominal ply thickness of 0.167 mm/ply and was manufactured using wet layup method with symmetrical [0-90] fiber orientation, which is a standard civil engineering industrial practice to strengthen concrete beams. Flat coupon tensile tests in accordance with ASTM D3039 were conducted to determine material properties of the carbon fiber–reinforced polymer (CFRP). The tensile modulus of the CFRP sheet obtained from the coupon tests are 244.6 and 238.1 GPa for 2-ply and 3-ply CFRP, respectively. The bond surface of the concrete blocks was roughened using an abrasive roughening grinder to remove surface mortar and expose the aggregate (Figure 9(a)). A two-part HUNT Epoxy HP-GPA with

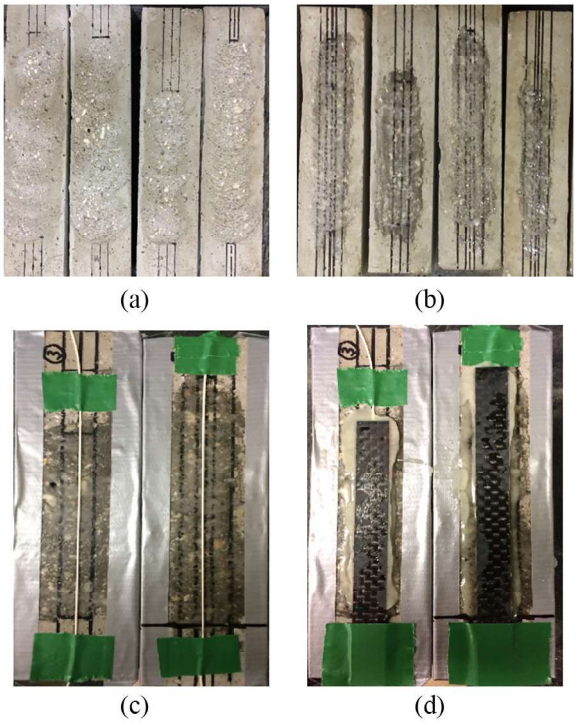

Figure 9. Sample preparation: (a) surface treatment, (b) surface after adhesive layer application, (c) placement of TL sensors in the adhesive layer, and (d) Finished beam with CFRP laminate applied on the concrete surface.

a shear strength of 20 MPa was used for bonding. Before bonding the fabric, a coat of epoxy was applied on the cleaned bonding area (Figure 9(b)). For samples with no sensors, the cured laminate was then placed on the adhesive layer after which pressure was applied to get as thin of an adhesive layer as possible. For samples with sensors, the TL sensor was placed on the first adhesive layer (Figure 9(c)) and another layer of adhesive was applied before placing the laminate on the adhesive layer after which pressure was applied. The finished beam with the application of CFRP laminate is shown in Figure 9(d). The list of test specimens is shown in Table 1. The first number in sample nomenclature corresponds to the bond length, the second number corresponds to the number of plies in the laminate, and the third variable *TL* represents the presence of the TL sensor in the adhesive layer. The width of the applied laminates was 25 mm. The experimental setup is shown in Figure 10. The fixture was manufactured in house where the two steel plates act as constraint to the concrete beam making it a *fixed* boundary condition. Four threaded rods were used to adjust the steel plates as per the beam height (length of the beam). Locking nuts were used to anchor the steel plates in place such that the there is no movement in the beam during testing. Modular mic from Sparkfun was used to record acoustic signatures upon cracking and onset of debonding for samples with embedded TL sensors. The TL emissions were recorded using a photomultiplier tube (PMT) sensor. Both the PMT and the modular mic were connected to NI USB 6210. The NI USB 6210 is an analog input output device that can record data at a rate of 250 kHZ. The continuous data acquisition was achieved using an in-house built MATLAB code at a rate of 10 kHz. The CFRP was pulled at a constant crosshead speed of 1 mm/min.

Table 1. Test specimens.

Sample	No. of plies	Bond length (L) (mm)
S150-2-TL	2	150
S150-3-TL	3	150
S200-2-TL	2	200
S200-3-TL	3	200
S150-2	2	150
S150-3	3	150
S200-2	2	200
S200-3	3	200

Finite element modeling

Single lap shear tests were simulated by means of a three-dimensional (3D) finite element (FE) model which took into account the actual geometry of the specimens using ABAQUS CAE. Half of the specimens were represented in the model due to symmetry along the longitudinal axis as can be seen in Figure 11. Simulations were restricted to the elastic region of the tests. Thus, the mechanical behavior of the composite, concrete, and the adhesive parts are considered linear and elastic. In addition, perfect bonding was considered for all interfaces, namely, FRP-adhesive and concrete-adhesive. The geometry of the FRP is modeled as 3D conventional shell with S4R element type. This is a conventional shell element quadrilateral that is a robust, general-purpose element that is suitable for a wide range of applications and converges to shear flexible theory for thick shells and classical theory for thin shells. The concrete and the adhesive were modeled as solids with C3D8R element type, which is a 8-node brick element with reduced integration. A fine mesh was created along the bondline of both the interfaces.

Results and discussion

Bond performance

The bond stress from a single lap shear test was evaluated by equation (2) as per ASTM 5868

$$Bond\ stress,\ \tau_{max} = \frac{P}{Bonded\ area} \tag{2}$$

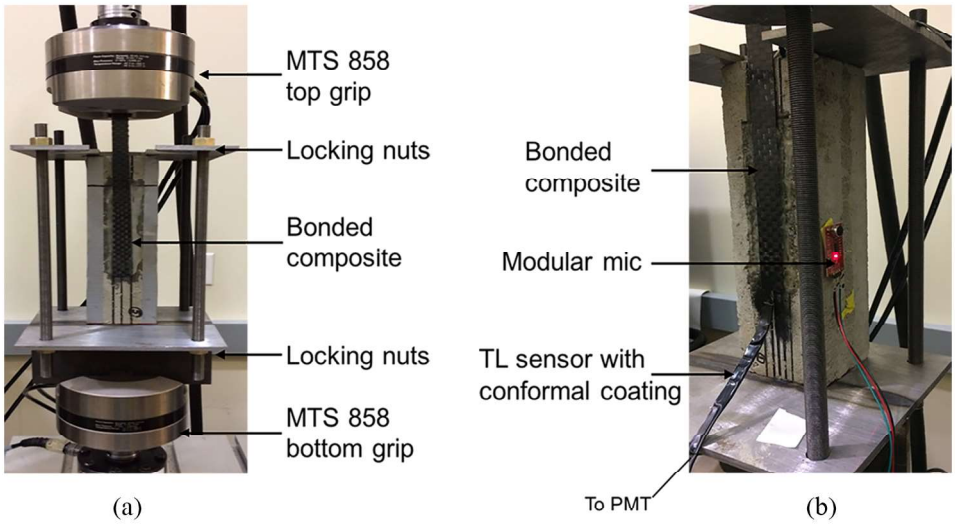

Figure 10. (a) Experimental setup for samples with no sensors and (b) experimental setup for samples with embedded sensors.

Table 2. Performance of control beams.

Sample	Adhesive thickness (mm)	Failure load (kN)	Bond stress (MPa)	Failure mode
S150-3	0.8	5.91	3.02	Adhesion
S150-2	0.79	4.38	2.24	Adhesion
S200-3	0.82	5.79	2.89	Adhesion
S200-2	0.8	6.63	3.35	Mixed mode

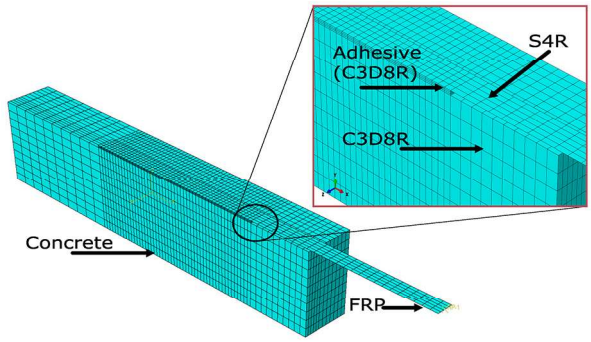

Figure 11. Geometry and meshing scheme in ABAQUS CAE.

Apart from the bond stresses, the failure modes of the beams were observed and compared to the failure modes of beams with sensors. The three phases of failure described in section "Stress transfer mechanism" were looked into for validity of the tests. The average thickness of the adhesive layer for the control samples observed was 0.80 mm. As explained by López-González et al. (2012), when using low-strength concrete members (f_c' of 20–40 MPa), the thickness of the adhesive is unrelated to the bond strength, as the concrete beam is the weakest component, which is the reason it was expected that the failure mode resulting in the ultimate failure will be debonding resulting from concrete peeling. However, the debonding failure mode is associated with other failure modes such as adhesion or cohesion failure mode based on the bond quality. There were two peculiar failure modes observed with the control beams, namely, adhesion failure and mixed-mode failure as seen in Figure 12(a). A mixed-mode failure mode is defined by adhesion failure of the FRP-adhesive interface accompanied with concrete peeling. The mixed-mode failure mode represents good adhesion between the structural components but considering concrete is the weakest member as explained by López-González, concrete peeling is evident. The mechanical performance of the control beam is shown in Table 2. The bond stress associated with mixed-mode failure mode was observed to be highest as compared to bond stresses in adhesion failure mode as seen in Figure 12(a) and (b). The average adhesive thickness observed in beams with sensors embedded in the adhesive layer was 1.47 mm. The beams showed similar performance to control beams with two distinct failure modes. Two beams failed with mixed-mode failure mode and were associated with highest bond stresses while adhesion failure mode was seen in two other beams (Table 3). Beam 200-2-TL showed higher bond stress even after failing in adhesion failure mode

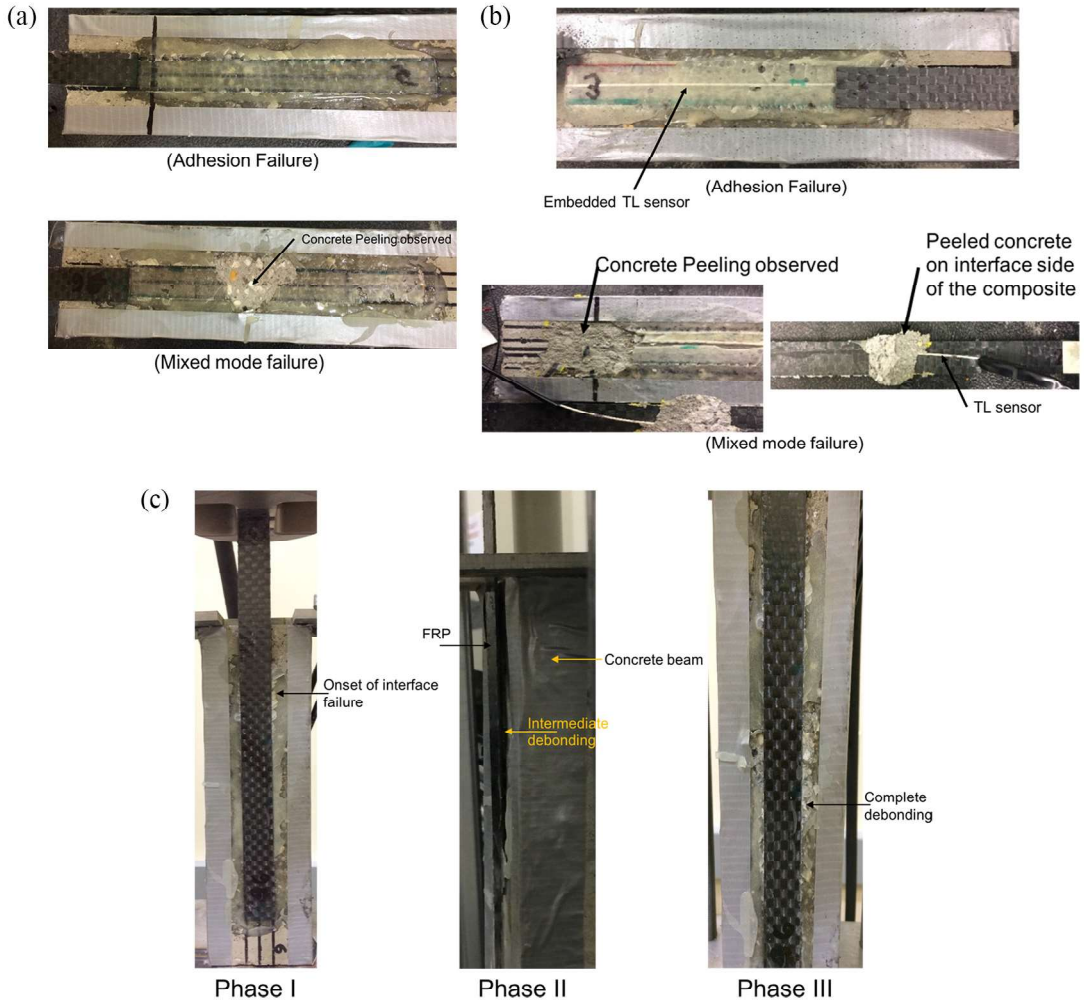

Figure 12. Failure modes observed in the experimentation: (a) typical failure modes observed in the control beams, (b) typical failure modes observed in the beams with embedded TL sensors, and (c) phases of failure that follow the theory explained in section "Stress transfer mechanism."

Table 3. Performance of beams with TL sensor.

Sample	Adhesive thickness (mm)	Failure load (kN)	Bond stress (MPa)	Failure mode
S150-3-TL	1.45	3.94	2.94	Adhesion
S150-2-TL	1.5	4.58	3.00	Mixed mode
S200-3-TL	1.5	6.61	3.34	Mixed mode
S200-2-TL	1.46	6.13	2.90	Adhesion

possibly because of the higher bond length which causes retardation in phase 2 and phase 3 failure as explained in section "Stress transfer mechanism" (Figures 13 and 14).

However, all three phases of failures were observed in the beams as shown in Figure 12(c). The three phases of failure are (1) onset of debonding at the concrete boundary condition followed by (2) crack propagation/intermediate debonding and (3) complete debonding at the end of the bonded region. The bond stresses for beams with embedded sensors are similar to the control beams because of the explanation given by Lau et al. (2001) that when you have a sensor embedded in the adhesive layer, a long embedment length of the sensor is recommended for effective shear stress transfer. The results show that the bond stresses are not affected by the inclusion of the TL sensor; however, further investigation is needed to cover the entire spectrum of failure modes as in this work results are from adhesion failure and mixed-mode failure modes.

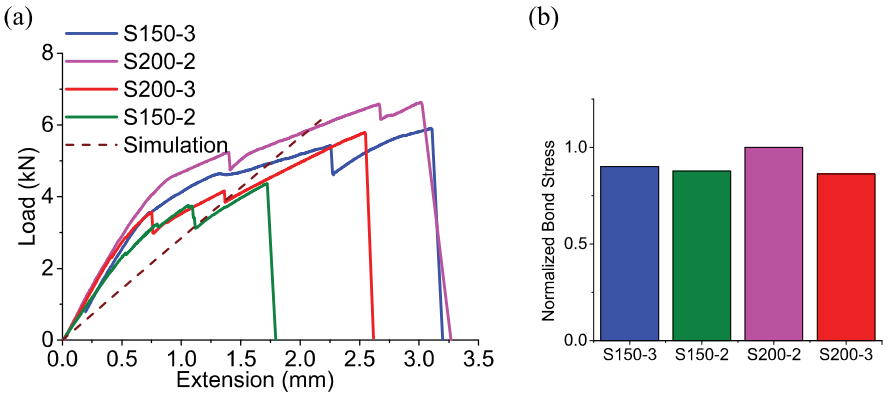

Figure 13. (a) Load versus displacement curve for control beams and (b) normalized bond stress for control beams.

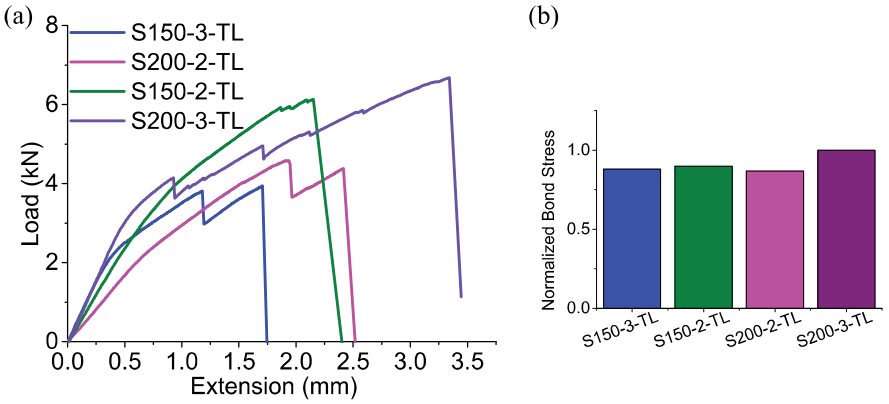

Figure 14. (a) Load versus displacement curve for beams with embedded sensors and (b) normalized bond stress for beams with sensors.

Numerical modeling performance

The evaluation of bond strength from experimental results depends on the quality of the bond, quality of the laminate, and the retrofitting process, but FE model is able to provide validation of the quality by providing useful insights into the bond behavior and performance (Figure 15). The preliminary model does not include TL sensor in the adhesive layer, but provides a basis for predicting the location of emission points.

The bond stress calculated using the theoretical equation (equation (2)) is 3.35 MPa, when compared to the average stress observed in the FE model, it shows very close correlation. The average stress from FE model is 3.85 MPa. The high stress concentration close to the loaded end results in phase I failure mode. The load displacement curve from FE model and experiments is shown in Figure 16. The maximum load from the FE results are in conjunction with the average maximum load observed in experiments. This suggests that the tested samples had good integrity and homogeneity

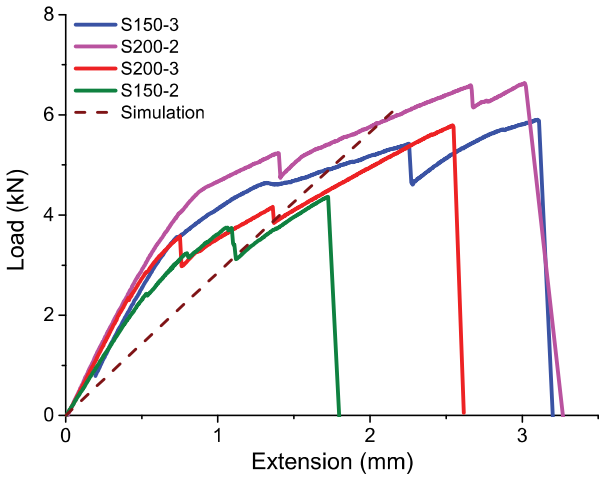

Figure 15. Load displacement curve comparison with FE simulation.

$$\tau = \frac{d\sigma_f}{dx} t_f \tag{3}$$

where σ_f is the axial stress in the plate and t_f is the thickness of the FRP plate. The local bond stress distributions found using equation (3) for the specimens in

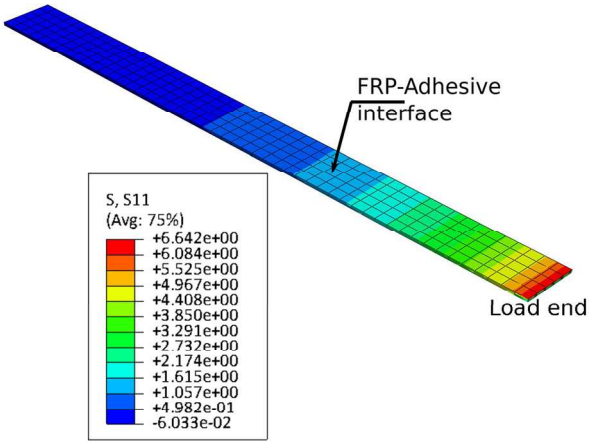

Figure 16. Shear stress in the adhesive layer which is equivalent to the bond stress.

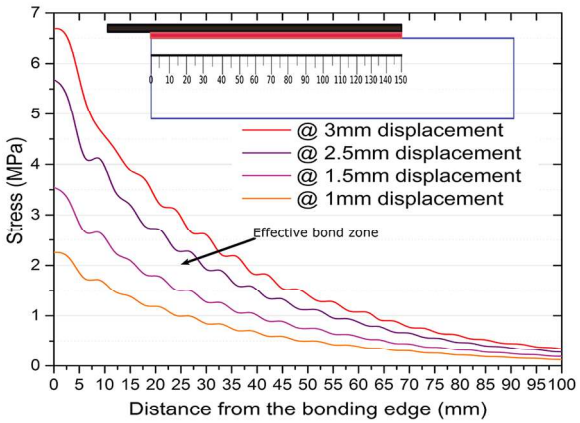

Figure 17. Shear stress in the adhesive layer over the bonded length showing the the effective bond zone.

this study is shown in Figure 17. No major fluctuations in the curves suggest that there are no interfacial cracks/stress concentrations in the concrete. The curves show clearly the effective bond zone at each loading level (Figure 17). The effective bond zone at each level of loading is defined herein as the length of the interface with significant bond stresses. The effective bond zone is around 80 mm from the 150 mm length of bonding. This suggests that the initial emissions are expected to occur as a result of stress transfer within the 80 mm zone as there is no significant cracking observed before phase I failure as explained in the following section.

TL sensor performance

The response of the TL sensors was recorded using a PMT which sends an arbitrary voltage signal that was recorded using a national instrument USB 6210 analog

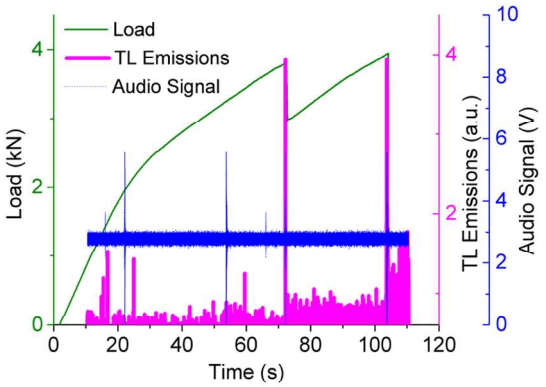

Figure 18. High correlation of the sensor seen with the audio signatures.

device. The responses were collected through an in-house written MATLAB code. The TL sensor ends were inserted into the periphery created in front of the complementary metal -oxide -semiconductor sensor in front of the PMT. The voltage from the PMT was continuously recorded during the test cycle. The TL emissions are characterized by a decay curve which was explained by Fontenot et al. (2012). The decay time is said to be around 350 μm and is independent of the amount of energy that the crystals experience.

The TL sensors showed TL signatures throughout the testing cycle and was passed through a noise filter in MATLAB. The signals showed good correlation with the audio signatures which represents the sensors sensitivity to minor cracks that occur during the test cycle as seen in Figure 18. Figure 18 shows a combination of the load curve, the audio signal, and the TL signal. The TL signals show similar correlation to the audio signal as observed in our previous work (Joshi et al., 2017). The work was conducted on ubiquitously distributed ZnS:Mn in a vinyl ester resin but nonetheless the emission mechanism show consistency whether ubiquitous or coated on an optical fiber as is in this work. The TL emissions showed consistent response for all four samples that consisted of embedded TL sensors. The TL signals display a burst in the intensity of luminescence upon the onset of debonding and major crack development as is seen in Figure 19. Chandra (1996) explained that the intensity is directly proportional to the stress induced upon the ZnS:Mn crystals, the stress in these experiments are in the form of high shear stresses that are a result of sudden energy release upon debonding and major cracking. This provides a unique capability to the TL sensors wherein the emissions provide information on micro and major cracks such as debonding.

The reason the authors claim that the TL signatures represent microcracking is because of the elastoluminescent property of the ZnS:Mn crystals. Figure 20 shows signatures even when there is no apparent drop in the load curve. The emissions suggest that there is a

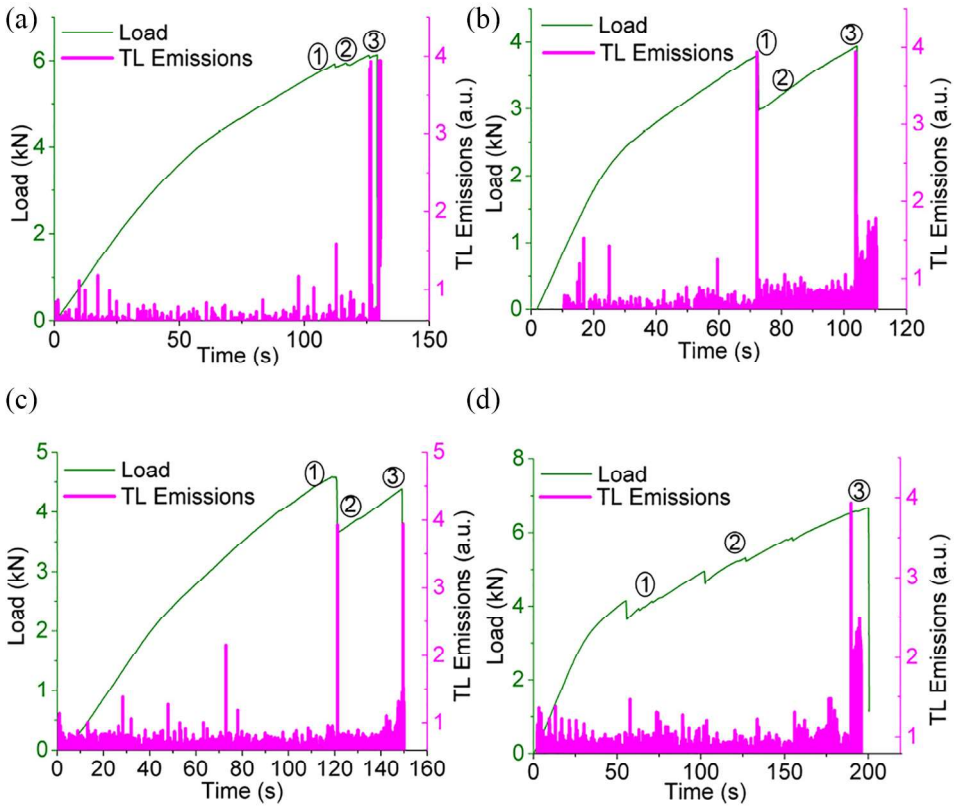

Figure 19. Response of the TL sensor for tested samples: (a) S150-2-TL, (b) S150-3-TL, (c) S200-2-TL, and (d) S200-3-TL.

structural change in the host material either in the form of microcracking or pure energy transfer. As there is no change in the slope of the load curve, the emissions can be said to be an occurrence of a combination of shear stresses that are induced on the sensor coating upon energy adsorption that causes the ZnS:Mn crystals to deform. This phenomenon was established on a single crystal by Sharma et al. (2011) where they explained the exhibitance of luminescence from ZnS:Mn upon deformation. However, in this study, we use an optical fiber that is coated with ZnS:Mn crystals and hence within the coating lies a distribution of crystals. The nominal sensor diameter is 1.2 mm that consists of a 1-mm-diameter optical fiber core with a 200 μm coating thickness. The shear stresses produced due to either microcracking or energy absorption are induced on the coating on the optical fiber that causes the emissions when the stresses are higher than 1 MPa. The bond stresses at which the debonding occurs are in the range of 2–4 MPa in addition to the amount of energy that is exerted upon the coating and that is why the luminescent intensity is about 200% higher on the onset of debonding. Thus, the sensor is able to differentiate between microcracks and major cracks just like an acoustic sensor. The critical advantage (Joshi et al., 2017) that the TL sensor has over the acoustic sensor is its ability to be embedded, thus providing information at the microlevel as compared to a surfacial level information which can be misleading.

Conclusion

TL optical fiber sensors were embedded in the adhesive layer of a CFRP laminate and concrete interface. When low-strength concrete member is used, there is no effect of the adhesive thickness on the strength of the bond which is observed through the mechanical single lap shear tests. A comparison of samples with embedded sensors to control beams showcase that the mode of failure is the dominant factor in determining the bond strength as it is observed that adhesion failure mode is a premature failure mode and thus is associated with low bond stresses. The mixed-mode failure mode which is close to an ideal failure mode is associated with higher stresses and leads to a violent failure. The TL sensors nonetheless are able to record and provide information on the damage state of the adhesive layer. The microcracking in the adhesive layer results in a sensor intensity in the range of 1–2 a.u. due to the transfer of small shear stresses resulting from microcracking or energy absorption from the host material. The TL intensities resulting from the onset of debonding are around 200% (2–4 a.u.) higher than intensities from microcracking which are a result of high shear stresses

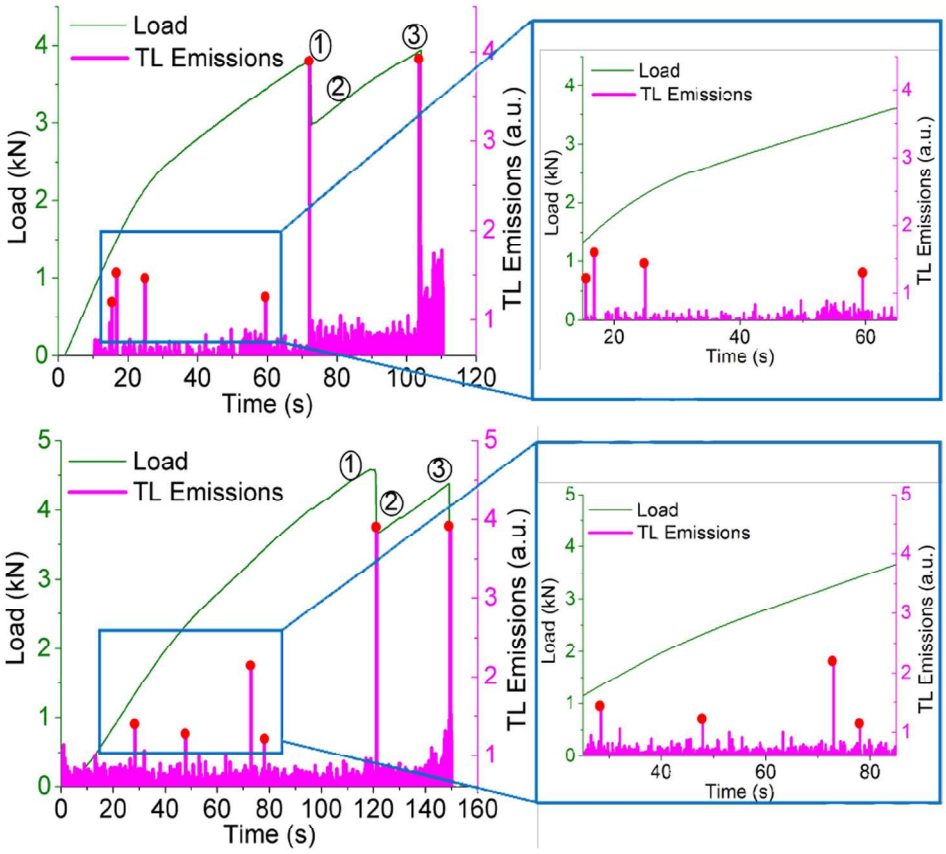

Figure 20. TL signatures representing structural change, red dots indicate the peak of TL intensity.

that are induced on the TL coating from the energy released upon debonding. This sensor provides a microscopic level of health monitoring compared to acoustic sensors which provide surfacial information which can be misleading. Other fiber optic sensors such as the FBG and BOTDR sensors require an external source of energy to receive information from the sensors. This sensor is a self-triggering sensor which does not require any other source of energy to produce information which makes it unique.

The future work will consist of optimizing the sensor diameter and correlating the TL intensity signatures to the stress-state condition of the adhesive layer. When fully developed, these sensors can be used in any material such as FRP composites for microdamage detection. Real-time failure detection of FRP-strengthened beams was successfully achieved and the retrofit damage-monitoring scheme aims at providing a tool to reduce the response time and decision making involved in the maintenance of deficient structures.

Declaration of conflicting interests

The author(s) declared no potential conflicts of interest with respect to the research, authorship, and/or publication of this article.

Funding

The author(s) received no financial support for the research, authorship, and/or publication of this article.

ORCID iD

Kunal Joshi https://orcid.org/0000-0003-3675-2581

References

Abdel Wahab M (2012) Fatigue in adhesively bonded joints: a review. *ISRN Materials Science* 2012: 746308 (25 pp.).

Alzetta G, Chudáček I and Scarmozzino R (1970) Excitation of triboluminescence by deformation of single crystals. *physica status solidi (a)* 1(4): 775–785.

ASTM D5868-01 (2014) Standard test method for lap shear adhesion for fiber reinforced plastic (FRP) bonding.

Banea M and Da Silva LF (2009) Adhesively bonded joints in composite materials: an overview. *Proceedings of the Institution of Mechanical Engineers, Part L: Journal of Materials Design and Applications* 223(1): 1–18.

Chandra B (1996) Luminescence induced by moving dislocations in crystals. *Radiation Effects and Defects in Solids* 138(1–2): 119–137.

Chandra B (1998) *Luminescence of Solids* (ed DR Vij). New York: Plenum Press.

Chandra B (2011) Development of mechanoluminescence technique for impact studies. *Journal of Luminescence* 131(6): 1203–1210.

Comer A, Katnam K, Stanley W, et al. (2013) Characterising the behaviour of composite single lap bonded joints using digital image correlation. *International Journal of Adhesion and Adhesives* 40: 215–223.

Curley A, Hadavinia H, Kinloch A, et al. (2000) Predicting the service-life of adhesively-bonded joints. *International Journal of Fracture* 103(1): 41–69.

Dickens T, Okoli O and Liang R (2008) *Harnessing Triboluminescence for Structural Health Monitoring of Composite Structures*. Tallahassee, FL: High Performance Materials Institute, FAMU-FSU College of Engineering.

Ehrhart B, Valeske B, Muller CE, et al. (2010) Methods for the quality assessment of adhesive bonded CFRP structures—a resume. In: *Proceedings of international symposium on NDT in aerospace*, Hamburg, pp. 22–24. Available at: http://2010.ndt-aerospace.com/Portals/aerospace 2010/BB/we5b2.pdf

Fontenot RS, Hollerman WA, Bhat KN, et al. (2012) Comparison of the triboluminescent properties for europium tetrakis and ZnS: Mn powders. *Journal of Theoretical and Applied Physics* 6(1): 1–9.

Higgins A (2000) Adhesive bonding of aircraft structures. *International Journal of Adhesion and Adhesives* 20(5): 367–376.

Joshi K, Frketic JB, Olawale D, et al. (2015a) Damage monitoring of CFRP retrofit using triboluminescent optical fiber sensors. In: *SPIE smart structures and materials + nondestructive evaluation and health monitoring*, San Diego, CA, 8–12 March, pp. 943520. Bellingham, WA: SPIE.

Joshi K, Frketic JB, Raley M, et al. (2015b) *Screening failure detection of structural composite systems: embedded triboluminescent structronic wires*. vol. 2, pp. 1737–1745.

Joshi K, Mishra S, Campbell C, et al. (2017) Light emitting composite beams during matrix cracking. *Journal of Composite Materials* 51: 4251–4260.

Lau KT, Yuan L, Zhou LM, et al. (2001) Strain monitoring in FRP laminates and concrete beams using FBG sensors. *Composite Structures* 51(1): 9–20.

López-González JC, Fernández-Gómez J and González-Valle E (2012) Effect of adhesive thickness and concrete strength on FRP-concrete bonds. *Journal of Composites for Construction* 16(6): 705–711.

Majumder M, Gangopadhyay TK, Chakraborty AK, et al. (2008) Fibre Bragg gratings in structural health monitoring present status and applications. *Sensors and Actuators A: Physical* 147(1): 150–164.

Okoli O and Olawale D (2016) Triboluminescent optical fiber sensor. US Patent 9,274,025. Available at: https://www.google.com/patents/US9274025

Sage I, Humberstone L, Oswald I, et al. (2001) Getting light through black composites: embedded triboluminescent structural damage sensors. *Smart Materials and Structures* 10(2): 332.

Sharma R, Bisen D, Brahme N, et al. (2011) Mechanoluminescence glow curve of ZnS: Mn nanocrystals prepared by chemical route. *Digest Journal of Nanomaterials and Biostructures* 6: 499–506.

Shenoy V, Ashcroft I, Critchlow G, et al. (2009) An investigation into the crack initiation and propagation behaviour of bonded single-lap joints using backface strain. *International Journal of Adhesion and Adhesives* 29(4): 361–371.

Smith ST and Teng J (2002a) FRP-strengthened RC beams. I: review of debonding strength models. *Engineering Structures* 24(4): 385–395.

Smith ST and Teng J (2002b) FRP-strengthened RC beams. II: assessment of debonding strength models. *Engineering Structures* 24(4): 397–417.

Teng J, Smith ST, Yao J, et al. (2003) Intermediate crack-induced debonding in RC beams and slabs. *Construction and Building Materials* 17(6): 447–462.

Tsai M and Morton J (1995) An experimental investigation of nonlinear deformations in single-lap joints. *Mechanics of Materials* 20(3): 183–194.

Wu YF and Jiang C (2013) Quantification of bond-slip relationship for externally bonded FRP-to-concrete joints. *Journal of Composites for Construction* 17(5): 673–686.

Wu Z, Yuan H and Niu H (2002) Stress transfer and fracture propagation in different kinds of adhesive joints. *Journal of Engineering Mechanics* 128(5): 562–573.

Xu C, Watanabe T, Akiyama M, et al. (1999) Preparation and characteristics of highly triboluminescent ZnS film. *Materials Research Bulletin* 34(10): 1491–1500.

Yuan H, Teng J, Seracino R, et al. (2004) Full-range behavior of FRP-to-concrete bonded joints. *Engineering Structures* 26(5): 553–565.